

Pareto-Front Engineering of Dynamical Sweet Spots in Superconducting Qubits

Zhen Yang,¹ Shan Jin,¹ Yajie Hao,¹ Guangwei Deng,^{1,*} Xiu-Hao Deng,^{2,†} Re-Bing Wu,^{3,‡} and Xiaoting Wang^{1,§}

¹*Institute of Fundamental and Frontier Sciences,*

University of Electronic Science and Technology of China, Chengdu 610051, China

²*Shenzhen International Quantum Academy, and Shenzhen Branch,*

Hefei National Laboratory, Shenzhen, 518048, China

³*Center for Intelligent and Networked Systems, Department of Automation, Tsinghua University, Beijing 100084, China*

(Dated: January 28, 2026)

Operating superconducting qubits at dynamical sweet spots (DSSs) suppresses decoherence from low-frequency flux noise. A key open question is how long coherence can be extended under this strategy and what fundamental limits constrain it. Here we introduce a fully parameterized, multi-objective periodic-flux modulation framework that simultaneously optimizes energy relaxation (T_1) and pure dephasing (T_ϕ), thereby quantifying the tradeoff between them. For fluxonium qubits with realistic noise spectra, our method enhances T_ϕ by a factor of 3-5 compared with existing DSS strategies while maintaining T_1 in the hundred-microsecond range. We further prove that, although DSSs eliminate first-order sensitivity to low-frequency noise, relaxation rate cannot be reduced arbitrarily close to zero, establishing an upper bound on achievable T_1 . At the optimized working points, we identify double-DSS regions that are insensitive to both DC and AC flux, providing robust operating bands for experiments. As applications, we design single- and two-qubit control protocols at these operating points and numerically demonstrate high-fidelity gate operations. These results establish a general and useful framework for Pareto-front engineering of DSSs that substantially improves coherence and gate performance in superconducting qubits.

I. INTRODUCTION

Superconducting qubits are among the most advanced platforms for quantum computation, with the transmon qubit being widely studied in both theory and experiment [1–17]. In parallel, the fluxonium qubit has emerged as a promising alternative, offering long coherence times and high anharmonicity [18–20]. Nevertheless, preserving quantum coherence remains a central challenge, because qubits inevitably couple to their environments. Extending coherence times and mitigating noise-induced errors are therefore critical goals for both fault-tolerant quantum computing and near-term noisy intermediate-scale quantum processors [21–24]. In fluxonium devices, dominant decoherence mechanisms include flux noise [25] and dielectric loss [26]. Several strategies have been developed to improve coherence, including operating at static sweet spots [27–31], applying dynamical decoupling techniques [32–36], and advancing materials and fabrication techniques [26, 37]. More recently, periodic flux modulation has been proposed to combine the advantages of static sweet spots and dynamical decoupling. This approach gives rise to dynamical sweet spots (DSSs), where the first-order sensitivity to low-frequency flux noise is suppressed, thereby improving both energy relaxation time (T_1) and pure dephasing time (T_ϕ). DSSs have since been explored extensively in both theory and experiment, demonstrating substantial

robustness to noise [38–47]. In transmons, they were introduced via single-tone parametric flux modulation [38], with two-tone drives later improving gate performance in experiments [39]. In fluxonium, Huang et al. [40] established Floquet-engineered continuous DSS families that support control and readout, with experiments reporting up to a 40-fold increase in coherence at such DSSs [41]. Subsequent studies have further expanded the DSS toolbox: longitudinal readout eliminates the adiabatic ramp in dispersive schemes [42]; tunable-complex-amplitude modulation [43] and commensurate two-tone modulation [44] further extend the control space and improve coherence times; two-tone modulation provides access to double-DSS operating points, for which analytic formulas on their locations which are useful for parameter selection [48]. Overall, DSSs have evolved from single-tone transmon implementations to Floquet-engineered fluxonium families, expanding control capabilities and boosting robustness.

Despite this progress, important limitations remain. At static sweet spots, qubits typically exhibit longer T_ϕ but shorter T_1 compared to points far from the sweet spot, reflecting an inherent trade-off between these two figures of merit. A similar competition arises in DSSs: the system parameters that maximize T_ϕ generally do not coincide with those that maximize T_1 [43]. Moreover, existing DSS schemes often restrict the modulation to pre-defined forms, such as single-tone or two-tone drives [40–44]. These constraints naturally raise the question: can coherence times T_1 and T_ϕ be optimized simultaneously under general periodic flux control, and what fundamental limits govern their maximum values?

To overcome the limitations of existing DSS approaches and to systematically determine both the op-

* gwdeng@uestc.edu.cn

† dengxiuhao@iqasz.cn

‡ rbwu@tsinghua.edu.cn

§ xiaoting@uestc.edu.cn

timal coherence times and their fundamental limits, we develop a fully parameterized multi-objective periodic-flux modulation framework for fluxonium qubits. This framework generalizes beyond conventional single- and two-tone drives by allowing arbitrary periodic flux modulations, thereby enlarging the search space for waveform design. Within this setting, we perform a multi-objective optimization of T_1 and T_ϕ and map out the resulting T_1 - T_ϕ Pareto front (PF), which makes the trade-off explicit and identifies optimal operating points. For realistic experimental parameters, the optimal solutions on this PF extend T_ϕ by factors of 3-5 compared with existing DSS strategies, while maintaining T_1 in the hundred-microsecond regime. By analyzing the PF, we find that relaxation times T_1 cannot be increased without bound under any periodic-flux modulation. Finally, the optimized PF also includes “double-DSS” regions that are simultaneously insensitive to both DC and AC flux, providing robust operating bands that are well suited for experiments. As applications, based on typical experimental parameters, we select a representative DSS on the PF to evaluate the impact of noise on gate fidelity in open quantum systems. Numerical results demonstrate a high-fidelity single-qubit X gate with 99.9993% fidelity under a 10 ns evolution, and a \sqrt{iSWAP} gate achieving 99.995% fidelity within 28 ns.

Unless otherwise stated, we focus on fluxonium qubits throughout this work, though similar techniques are also applicable to transmon devices. This paper is organized as follows. Section II introduces the dynamics of fluxonium qubits under general periodic modulation and establishes the connection between tunable parameters and decoherence rates. Section III describes the multi-objective numerical optimization procedure to simultaneously optimize T_1 and T_ϕ , and reports the T_1 - T_ϕ Pareto front, along with the identification of double-DSS regions. Section IV demonstrates the realization of high-fidelity quantum gates at optimal DSS operating points.

II. FLUXONIUM QUBITS UNDER GENERAL PERIODIC MODULATION

Under general periodic modulation, the dynamics of fluxonium qubits are well described within the Floquet framework. This formalism allows us to analyze the system-bath interaction and to derive the associated decoherence rates in the presence of low-frequency $1/f$ flux noise and dielectric loss.

A. System Hamiltonian

The Hamiltonian of the fluxonium system is given by [49]

$$H_q(t) = 4E_C\hat{n}^2 + \frac{1}{2}E_L[\hat{\phi} + \phi_{\text{ext}}(t)]^2 - E_J \cos \hat{\phi}, \quad (1)$$

where E_C , E_L , and E_J denote the capacitive, inductive, and Josephson energies, respectively. $\hat{n} = Q/(-2e)$ represents the Cooper-pair number operator, while $\hat{\phi} = 2\pi\Phi/\Phi_0$ is the dimensionless flux operator. Here, $\Phi_0 = h/(2e)$ is the magnetic flux quantum, where h is Planck’s constant. The charge operator Q and the flux operator Φ satisfy the canonical commutation relation $[\Phi, Q] = i\hbar$, which leads to $[\hat{n}, \hat{\phi}] = i$. In this work, we discuss the most general form of the external periodic flux drive:

$$\phi_{\text{ext}}(t) = \phi_{\text{dc}} + \phi_{\text{ac}}P(t), \quad (2)$$

where ϕ_{dc} is the static DC component and $P(t)$ is the periodic AC component with frequency ω_d . The real-valued periodic function $P(t)$ can be expanded in Fourier series as $P(t) = \sum_n p_n e^{in\omega_d t}$. The Fourier coefficients $p_n \in \mathbb{C}$ are treated as trainable parameters, subject to the Hermiticity condition $p_{-n} = p_n^*$ to ensure that $P(t)$ is real. Consequently, the Hamiltonian is time-periodic, satisfying $H_q(t) = H_q(t + T)$ with period $T = 2\pi/\omega_d$.

At a DC flux bias of $\phi_{\text{dc}} = \pi$, the fluxonium system operates at the so-called static sweet spot, where the qubit energy splitting is first-order insensitive to low-frequency flux noise [40]. In contrast, away from this bias point (i.e., at an off-sweet-spot such as $\phi_{\text{dc}} = 1.03\pi$), the system regains flux sensitivity, which can be exploited for controlled modulation at the expense of increased susceptibility to noise. Restricting the dynamics to the lowest two eigenstates at the chosen static sweet spot, $\{|\tilde{g}\rangle, |\tilde{e}\rangle\}$, the effective Hamiltonian takes the form [43]

$$H_q(t) = \frac{\Delta}{2}\sigma_x + \frac{B}{2}\sigma_z + AP(t)\sigma_z, \quad (3)$$

where Δ is the energy gap between $|\tilde{g}\rangle$ and $|\tilde{e}\rangle$. The coefficients are defined as $A = E_L\phi_{\text{ac}}\tilde{\varphi}_{ge}$, $B = 2E_L(\phi_{\text{dc}} - \pi)\tilde{\varphi}_{ge}$, and $\tilde{\varphi}_{ge} = |\langle\tilde{g}|\hat{\varphi}|\tilde{e}\rangle|$. The effective Pauli operators in the qubit subspace are defined as $\sigma_x = |\tilde{e}\rangle\langle\tilde{e}| - |\tilde{g}\rangle\langle\tilde{g}|$ and $\sigma_z = |\tilde{g}\rangle\langle\tilde{e}| + |\tilde{e}\rangle\langle\tilde{g}|$.

Since the effective Hamiltonian $H_q(t)$ contains an explicit time-periodic drive, the system’s dynamics are governed by the time-dependent Schrödinger equation with a periodic Hamiltonian. In this setting, Floquet theory [50] provides a natural framework for describing the solutions. Specifically, the wavefunctions can be expressed in the Floquet form

$$|\psi_\pm(t)\rangle = e^{-i\epsilon_\pm t} |\omega_\pm(t)\rangle, \quad (4)$$

where ϵ_\pm are the quasienergies, and $|\omega_\pm(t)\rangle$ are the corresponding Floquet states, which are periodic in time with the same period as $H_q(t)$. The quasienergies and Floquet states are obtained by solving the Floquet equation [51]

$$\left[H_q(t) - i\frac{\partial}{\partial t} \right] |\omega_\pm(t)\rangle = \epsilon_\pm |\omega_\pm(t)\rangle. \quad (5)$$

By expanding the Hamiltonian and Floquet states in Fourier components, we have $H_q(t) = \sum_{n \in \mathbb{Z}} H_q^{[n]} e^{-in\omega_d t}$

and $|\omega_{\pm}(t)\rangle = \sum_{k \in \mathbb{Z}} |\omega_{\pm}^{[k]}\rangle e^{-ik\omega_d t}$, and the operator $[H_q(t) - i\frac{\partial}{\partial t}]$ can be recast as an infinite-dimensional Floquet matrix \mathcal{H}_F in the basis $\{|\omega_{\pm}^{[k]}\rangle, k \in \mathbb{Z}\}$ [43]:

$$\mathcal{H}_F = \begin{pmatrix} \ddots & \vdots & \vdots & \vdots & \ddots \\ \cdots & H_q^{[0,-1]} & H_q^{[-1]} & H_q^{[-2]} & \cdots \\ \cdots & H_q^{[1]} & H_q^{[0,0]} & H_q^{[-1]} & \cdots \\ \cdots & H_q^{[2]} & H_q^{[1]} & H_q^{[0,1]} & \cdots \\ \ddots & \vdots & \vdots & \vdots & \ddots \end{pmatrix} \quad (6)$$

The off-diagonal blocks are $H_q^{[n \neq 0]} = A p_n \sigma_z$, and the diagonal blocks read $H_q^{[0,k]} = H_q^{[0]} + k \omega_d \mathbb{I}$ where $H_q^{[0]} = \frac{\Delta}{2} \sigma_x + (\frac{B}{2} + p_0 A) \sigma_z$. Diagonalizing \mathcal{H}_F yields the quasienergies, corresponding to the pair of eigenvalues with the smallest absolute value, while the Floquet states are obtained from the associated eigenvectors.

B. Noise and Decoherence Rates

For completeness, we begin by reviewing the derivation of decoherence rates in a fluxonium qubit subject to environmental noise. The total Hamiltonian is

$$H(t) = H_q(t) + H_B + H_{\text{int}}, \quad (7)$$

where H_q and H_B describe the qubit and bath Hamiltonians, respectively, and $H_{\text{int}} = \sigma_z \beta$ captures their interaction. To analyze the system dynamics, we move into the rotating frame defined by $U_q(t) \otimes U_B(t)$, where $U_q(t) = \mathcal{T} \exp \left[-i \int_0^t H_q(t') dt' \right]$ and $U_B(t) = \exp(-iH_B t)$. Here \mathcal{T} is the time-ordering operator. In this frame, the interaction Hamiltonian becomes $H_{\text{int}}(t) = \sigma_z(t) \beta(t)$, with $\sigma_z(t) = U_q^\dagger(t) \sigma_z U_q(t)$ and $\beta(t) = U_B^\dagger(t) \beta U_B(t)$, which encodes the system's time-dependent sensitivity to noise.

In the Floquet state basis $\{|\omega_{\pm}(t)\rangle\}$, we introduce the operator basis $\{\tau_j(t) | j = z, \pm\}$, where $\tau_z(t) = |\omega_+(t)\rangle \langle \omega_+(t)| - |\omega_-(t)\rangle \langle \omega_-(t)|$, and $\tau_+(t) = \tau_-^\dagger(t) = |\omega_+(t)\rangle \langle \omega_-(t)|$. In this representation, $\sigma_z(t)$ admits a Bohr-frequency decomposition, $\sigma_z(t) = \sum_{\omega=0,\pm\Omega} \sigma_z(\omega)$, with components $\sigma_z(0) = \frac{1}{2} \tau_z(0) \text{Tr}[\sigma_z \tau_z(t)]$ and $\sigma_z(\pm\Omega) = \tau_{\pm}(0) e^{\pm i\Omega t} \text{Tr}[\sigma_z \tau_{\mp}(t)]$. Here, $\Omega = \epsilon_+ - \epsilon_-$ denotes the quasienergy gap. The bath operator $\beta(t)$ determines the noise correlation function, $C(t) = \text{Tr}[\beta(t) \beta(0) \rho_B]$, whose Fourier transform yields the noise spectral density $S(\omega)$.

The reduced dynamics of the qubit are governed by the second-order time-convolutionless master equation [52]:

$$\frac{d}{dt} \rho(t) = i [\rho(t), H_{LS}(t)] + \sum_{\omega} \gamma(\omega, t) \mathcal{D}[\sigma_z(\omega)] \rho(t), \quad (8)$$

where Lamb-shift Hamiltonian $H_{LS}(t)$ is $\sum_{\omega} \mathcal{S}(\omega, t) \sigma_z^\dagger(\omega) \sigma_z(\omega)$, dissipator $\mathcal{D}[c] \rho \equiv c \rho c^\dagger -$

$\frac{1}{2} \{c^\dagger c, \rho\}$, and coefficients $S(\omega, t) = \text{Im}[\Gamma(\omega, t)]$, $\gamma(\omega, t) = 2 \text{Re}[\Gamma(\omega, t)]$ and $\Gamma(\omega, t) = \int_0^t ds e^{i\omega s} C(s)$. Expanding the periodic coefficients in Fourier harmonics, $\text{Tr}[\sigma_z \tau_j^\dagger(t)] = \sum_{k \in \mathbb{Z}} g_j^{[k]} e^{-ik\omega_d t}$ ($j = z, \pm$), the time-dependent decoherence rates take the form

$$\gamma_j(t) = \frac{1}{a_j} \int_{-\infty}^{+\infty} d\omega \left[\sum_k \frac{t}{\pi} \text{sinc}((\omega + \omega_{k,j})t) |g_j^{[k]}|^2 \right] S(\omega), \quad (9)$$

where $a_z = 4$, $a_{\pm} = 1$, $\omega_{k,z} = -k\omega_d$, $\omega_{k,\pm} = \pm\Omega - k\omega_d$, and Fourier coefficients

$$g_j^{[k]} = \frac{1}{b_j T} \int_0^T dt \text{Tr}[\sigma_z \tau_j^\dagger(t)] e^{ik\omega_d t}, \quad (10)$$

with $b_z = 2$, $b_{\pm} = 1$. For sufficiently long time ($t \gg 1/\omega_{k,j}$), the rates converge to time-independent values,

$$\gamma_z = \frac{1}{4} \sum_k |g_z^{[k]}|^2 S(k\omega_d), \quad \gamma_{\pm} = \sum_k |g_{\pm}^{[k]}|^2 S(k\omega_d \mp \Omega). \quad (11)$$

In practice, decoherence in fluxonium qubits is often dominated by $1/f$ flux noise and dielectric loss noise [29, 53, 54], with spectral density

$$S(\omega) = A_f^2 \left| \frac{2\pi}{\omega} \right| + \kappa(\omega, \mathcal{T}) A_d \left(\frac{\hbar\omega}{2\pi} \right)^2, \quad (12)$$

where A_f and A_d are the respective amplitudes. The thermal factor is $\kappa(\omega, \mathcal{T}) = \frac{1}{2} \left| \coth \left(\frac{\hbar\omega}{2k_B T} \right) + 1 \right|$. To regularize the infrared divergence of $1/f$ noise, we introduce cutoffs $\omega_{\text{ir}} = 1 \text{ Hz}$ and $\omega_{\text{uv}} = 3 \text{ GHz}$ following Ref. [55]. Under this model, the pure dephasing rate γ_z and energy relaxation rate γ_{\pm} are [43]:

$$\begin{aligned} \gamma_z &= \frac{1}{2} |g_z^{[0]}| A_f \sqrt{2 |\ln(\omega_{\text{ir}} t_m)|} + \frac{1}{4} \sum_{k \neq 0} |g_z^{[k]}|^2 S(k\omega_d), \\ \gamma_{\pm} &= \sum_{k \in \mathbb{Z}} |g_{\pm}^{[k]}|^2 S(k\omega_d \mp \Omega), \end{aligned} \quad (13)$$

where $\sqrt{|\ln(\omega_{\text{ir}} t_m)|} \approx 4$ since ω_{ir} is much smaller than the inverse timescale t_m [31, 56].

Finally, based on γ_{\pm} and γ_z , one can define the two types of coherence times, the energy relaxation time T_1 and pure dephasing time T_{ϕ} :

$$T_1 = \frac{1}{\gamma_+ + \gamma_-} \equiv \frac{1}{\gamma_1}, \quad T_{\phi} = \frac{1}{\gamma_z} \quad (14)$$

where $\gamma_1 = \gamma_+ + \gamma_-$. Operating the fluxonium system at the DSSs will help improve both coherence times in general. The next question is how to locate the DSSs given the general form of the periodic flux drive $\phi_{\text{ext}}(t) = \phi_{\text{dc}} + \phi_{\text{ac}} P(t)$.

III. IMPROVING COHERENCE TIMES VIA PARETO-FRONT OPTIMIZATION

For quantum computing applications, we aim to maximize both coherence times T_1 and T_ϕ , which is equivalent to minimizing both energy relaxation rate γ_1 and dephasing rate γ_z . In this section, under the most general periodic flux drive

$$\phi_{\text{ext}}(t) = \phi_{\text{dc}} + \phi_{\text{ac}} \sum_n p_n e^{i n \omega_d t}, \quad (15)$$

we show how to simultaneously optimize both γ_1 and γ_z under the DSS framework.

A. Joint optimization of γ_1 and γ_z

Under the general periodic flux modulation function $\phi_{\text{ext}}(t)$, the Floquet states $|\omega_j(t)\rangle$ depend explicitly on the modulation parameters $\{p_n\}$, and different parameter choices lead to distinct decoherence behaviors. We aim to solve the following bi-objective optimization problem:

$$\min_{\{p_n\}} (\gamma_1, \gamma_z), \quad (16)$$

subject to the normalization condition

$$\sum_{k \in \mathbb{Z}} \left(\frac{1}{2} \left| g_+^{[k]} \right|^2 + \frac{1}{2} \left| g_-^{[k]} \right|^2 + \left| g_z^{[k]} \right|^2 \right) = 1. \quad (17)$$

In a general multi-objective optimization problem, there is no single solution that simultaneously minimizes all objectives. Improving one objective often worsens another. The Pareto set is defined as the collection of parameter choices where neither γ_1 nor γ_z can be improved without sacrificing the other. Accordingly, the Pareto Front (PF) is defined as the curve you see when you plot all these trade-offs: it shows the best balance between γ_1 or γ_z . Consequently, solving a multi-objective optimization problem is often formulated as identifying and calculating the PF.

We note that gradient-based optimization methods may be impractical here: although they often converge faster, they require gradients with respect to $\{p_n\}$. Analytic gradients are difficult to obtain because each evaluation of the objective needs diagonalization of the truncated Floquet matrix, so numerical gradient estimates (e.g., finite differences) become computationally expensive as the parameter dimension grows. Moreover, the normalization condition Eq. (17) implies an inherent trade-off between γ_1 and γ_z . These considerations motivate the use of heuristic, population-based multi-objective algorithms, such as genetic algorithms [57].

Our approach begins by randomly initializing a population of M candidate solutions, each associated with an objective vector (γ_1, γ_z) . At each generation, this population serves as the parent pool to produce M

Algorithm 1. *Multi-objective optimization of decoherence rates*

Stage I — Evolutionary search

S1: Initialize a population of M individuals with random parameters $\{p_n\}$.

S2: For each generation do:

S2.1: Evaluate all individuals to obtain objective vectors (γ_1, γ_z) .

S2.2: Use the entire current population as the parent pool.

S2.3: Apply crossover and mutation to generate M offspring.

S2.4: Merge parents and offspring (size $2M$); apply an environmental-selection procedure to retain M individuals for the next generation.

S2.5: Check stopping condition.

S3: Output the non-dominated solutions of the final population as the run-level PF.

Stage II — PF aggregation

S4: Repeat Stage I to obtain multiple run-level PFs.

S5: Aggregate all run-level PF into a combined set.

S6: Perform non-dominated sorting and remove any dominated solution.

S7: Output the non-dominated solution as the aggregated PF.

offspring through variation, crossover, and mutation. After variation, an environmental selection step chooses which individuals survive to the next generation. The choice of selection mechanism determines the class of multi-objective optimization algorithm used. This generate-combine-select loop is iterated until a stopping condition is met (e.g., a fixed number N of generations, or convergence of a performance metric). At termination, the algorithm returns the set of non-dominated solutions from the final population as its PF, where dominance is defined as: solution A dominates B if A is no worse in every objective and strictly better in at least one.

In general, an analytical expression for the PF is generally unavailable. To obtain a more robust approximation, we run different multi-objective algorithms and merge their outputs to produce a collection of candidate PFs. Then we aggregate the non-dominated solutions from these fronts, and remove any solution that is dominated by another solution. The remaining non-dominated solutions aggregate into a curve, called the aggregated PF, which we treat as the final optimal solutions of the multi-objective optimization problem. The full procedure is summarized in Algorithm 1. Specifically, we draw on a pool of over 30 multi-objective optimization algorithms for Algorithm 1, including NSGA2 [57], SPEA2 [58], tDEA [59], IBEA [60], HypE [61], MOEA/D [62], ENS-MOEA/D [63], etc. For implementation details of the algorithms and the corresponding simulation we refer the reader to Ref. [64]. In our simulations, each algorithm is considered to converge when both the number and position of the non-dominated solutions on the PF show no

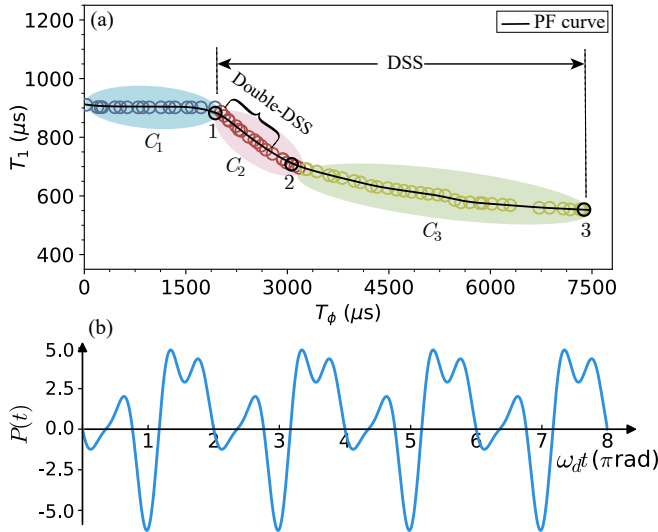


FIG. 1. (a) Aggregated PF with Fourier truncation $n = 4$, obtained by aggregating the run-level PFs from ENS-MOEA/D, HypE, SPEA2, and tDEA followed by a final non-dominated sort. Shaded lobes $C_1 - C_3$ indicate sub-regions preferentially explored by different algorithms. Working Point 1 marks the onset of the DSS region. The bracketed segment in C_2 , labeled “Double-DSS,” indicates the region where candidate double-DSS points occur. (b) Time-domain modulation for Working Point 2: $P(t) = \sum_n p_n e^{in\omega_d t}$, defining $\phi_{\text{ext}}(t) = \phi_{\text{dc}} + \phi_{\text{ac}} P(t)$.

significant change between successive generations. Here, we adopt numerical stopping criteria rather than relying on analytic convergence, due to the absence of analytical expressions for the Pareto front. To ensure a fair comparison across algorithms, the number of iterations is fixed at $N = 2000$ for all runs.

Different optimization algorithms explore complementary regions of the objective space. Among them, ENS-MOEA/D, HypE, SPEA2 and tDEA collectively produces a more comprehensive PF. We therefore combine the run-level PFs from these four algorithms to obtain the aggregated PF via a final non-dominated sorting. The resulting PF, shown in Fig. 1(a), illustrates the trade-off between the two optimization objectives γ_1 and γ_z , corresponding to the trade-off between T_1 and T_ϕ . Based on its relation to the DSSs, the aggregated PF can be divided into three distinct segments, C_1 , C_2 , and C_3 . As discussed in the next subsection, points on C_2 and C_3 are DSSs, and a segment of C_2 corresponds to the *double-DSSs*. A more detailed analysis of the aggregated PF is provided in Supplementary Note.

The aggregated PF indicates that our arbitrary-periodic flux-modulation approach attains longer coherence times than previously reported DSS schemes. We mark three representative working points on the PF in Fig. 1(a); their corresponding modulation parameters are provided in TABLE S1 in Supplementary Note. At Working Point 2 the energy relaxation time T_1 is com-

Working points	T_1 (μs)	T_ϕ (μs)
Off static sweet spot	940	1
DSS-1	877	2036
DSS-2	711	3035
DSS-3	553	7398
Static sweet spot	430	$> 10^4$
DSS in Ref. [40]	590	1200
DSS in Ref. [43]	718	2339

TABLE I. Coherence times T_1 and T_ϕ for representative operating points. We label three PF points discussed in Fig. 1 as DSS 1-3. (From the analysis below, these three working points satisfy the DSS conditions.) “Static sweet spot” refers to $\phi_{\text{ext}} = \pi$, where first-order sensitivity to DC flux noise vanishes and $T_\phi \rightarrow \infty$. “Off static sweet spot” uses $\phi_{\text{dc}} = 1.03\pi$ as in Ref. [43] and is included for comparison. The literature rows reproduce coherence reported previously DSS work.

parable to the 718 μs reported for the tunable-complex-amplitude scheme [43], while the dephasing time reaches $T_\phi = 3035$ μs. At Working Point 3 the dephasing time attains $T_\phi = 7398$ μs, roughly three- to five-fold larger than the values reported in earlier DSS works [40, 43]. The corresponding energy relaxation time at Working Point 3 is $T_1 = 553$ μs, which also exceeds the static sweet spot value $T_1 = 430$ μs. We summarize these results in Table I and illustrate the periodic modulation used at Working Point 2 as an example in Fig. 1(b).

In simulations, we truncate infinite-dimensional objects to finite size, such as the Fourier-coefficient set p_n and the Floquet matrix. Specifically, the Floquet matrix is truncated to dimension $3n$, which confines the numerical error in the computed Floquet states to below 10^{-10} (see FIG. S3 in Supplementary Note). We tested Fourier truncation orders $n = 1, \dots, 5$ and found that $n = 4$ yields the most complete PF for our parameter set. Accordingly, this section presents results for $n = 4$ only, while results for other n are given in FIG. S2 in Supplementary Note. For each p_n , the real and imaginary parts are constrained to lie in $[-1, 1]$, whereas the zeroth coefficient p_0 is restricted to $[0, 1]$. Because p_0 controls the effective DC flux ϕ_{dc} , permitting $p_0 \leq 0$ could return the system to a static sweet spot; we therefore exclude such values. The drive frequency is set in $\omega_d \in [0.5\Omega_{ge}, 1.5\Omega_{ge}]$. The device parameters are $E_C/(2\pi) = 1$ GHz, $E_L/(2\pi) = 0.79$ GHz, and $E_J/(2\pi) = 4.43$ GHz. The noise parameters are $A_d = \pi^2 \tan(\delta_C) |\tilde{\varphi}_{01}|^2 \hbar / E_C$ and $A_f = 2\pi\delta_f E_L |\tilde{\varphi}_{01}|$, with $\tan(\delta_C) = 1.1 \times 10^{-6}$, $\delta_f = 1.8 \times 10^{-6}$, and temperature $\mathcal{T} = 15$ mK.

B. Identifying DSS and Double-DSS

A DSS is an operating point where the quasienergy gap is first-order insensitive to the DC flux, i.e. $\partial\Omega/\partial\phi_{\text{dc}} \approx 0$. In our multi-objective periodic-flux modulation frame-

work we search for working points that minimize coherence rates. This search naturally uncovers DSS. The reason is that the dephasing objective γ_z depends on the coupling coefficient $g_z^{[0]}$ appearing in Eq. (13). Perturbation theory indicates that $\partial\Omega/\partial\phi_{dc}$ scales with $|g_z^{[0]}|$ [40]. Moreover, under the rotating-wave approximation the $k = 0$ Fourier component $|g_z^{[0]}|$ typically dominates the family $\{|g_z^{[k]}| : k \in \mathbb{Z}\}$, since other components carry rapidly oscillating factors $e^{ik\omega_d t}$ that average out. Consequently, minimizing γ_z steers the optimization toward points with small $|g_z^{[0]}|$, i.e., toward DSSs.

Our optimization results show that all working points to the right of Working Point 1 in Fig. 1(a) satisfy $|g_z^{[0]}| < 10^{-4}$. Using this threshold, this entire region can be regarded as a DSS regime. Fig. 1(a) also exhibits the existence of an upper bound on T_1 . In fact, according to Eq. (S1) in Supplementary Note, $\gamma_1 = \sum_{k \in \mathbb{Z}} |g_{\pm}^{[k]}|^2 \tilde{S}(k\omega_d - \Omega)$, the value of γ_1 is determined by two factors: the symmetrized noise spectrum $\tilde{S}(\omega) = S(\omega) + S(-\omega)$ and the filter weights $|g_{\pm}^{[k]}|^2$, $k \in \mathbb{Z}$. First, $\tilde{S}(\omega)$ itself possesses a lower bound, thus it imposes an upper bound on T_1 . Second, when the system is operated at DSS, $\sum_k |g_{\pm}^{[k]}|^2$ can be further rescaled, which yields a new upper bound to T_1 . We formalize these two upper bounds in Theorem 1. A rigorous proof is given in Supplementary Note.

Theorem 1. *Under the general periodic flux drive, the energy relaxation time T_1 is bounded by $T_{UB}^{(1)}$:*

$$T_1 \leq T_{UB}^{(1)} \equiv \frac{\sqrt{\pi}}{2A_f \sqrt{A_d \omega_d} \left\| \frac{\Omega}{\omega_d} \right\|_{\mathbb{R}/\mathbb{Z}}^{\frac{1}{2}} \sum_{k \in \mathbb{Z}} |g_{\pm}^{[k]}|^2}. \quad (18)$$

In particular, if the system is operated at the DSS, T_1 is bounded by $T_{UB}^{(2)}$:

$$T_1 \leq T_{UB}^{(2)} \equiv \frac{3\sqrt{\pi}\omega_d^2}{2A_f (A_d \omega_d)^{\frac{1}{2}} \left\| \frac{\Omega}{\omega_d} \right\|_{\mathbb{R}/\mathbb{Z}}^{\frac{1}{2}} |3\omega_d^2 - \pi^2 \Delta^2|}. \quad (19)$$

where $\|x\|_{\mathbb{R}/\mathbb{Z}} = \min_{k \in \mathbb{Z}} |x - k|$ refers to the distance between x and the nearest integer.

The bound $T_{UB}^{(1)}$ is universal: it holds for any choice of the external periodic flux $\phi_{ext}(t)$ and therefore applies broadly. However, bound $T_{UB}^{(1)}$ generally must be evaluated numerically, because the filter coefficients $|g_{\pm}^{[k]}|$ are determined by the Floquet solution. By contrast, the bound $T_{UB}^{(2)}$ admits to a closed-form expression when the quasienergy gap Ω is obtained analytically by perturbation theory, for example single- or two-tone driv-

ing [40, 48]. Particularly, combining the optimization condition $w_d \in [0.5\Omega_{ge}, 1.5\Omega_{ge}]$, the bound $T_{UB}^{(2)}$ reduces to a uniform upper bound which is independent of the flux modulation.

Above, the DSSs we find on the aggregated PF are insensitive to DC flux noise, but may be sensitive to AC flux noise. These points are referred to as single-DSSs. As noted in Ref. [41], the applied AC flux is itself subject to low-frequency fluctuations, which can introduce additional decoherence channels. Our method can also identify a distinct class of working points, referred to as the *double-DSSs*, where the qubit transition frequency is, to first order, insensitive to both DC and AC flux variations. Formally, the double-DSSs satisfy $\frac{\partial\Omega}{\partial\phi_{dc}} \approx 0$, $\frac{\partial\Omega}{\partial\phi_{ac}} \approx 0$. To examine whether the double-DSSs appear on the aggregated PF, we derive an equivalent, easily evaluated criterion for $\partial\Omega/\partial\phi_{ac}$ using first-order perturbation theory (see Supplementary Note for details):

$$\frac{\partial\Omega}{\partial\phi_{ac}} \approx \sum_{k=-\infty}^{\infty} p_k g_z^{[k]}, \quad (20)$$

so that the double-DSS conditions can be rewritten in the compact form $g_z^{[0]} \approx 0$, $\sum_{k=-\infty}^{\infty} p_k g_z^{[k]} \approx 0$. To identify the working points on PF with reduced sensitivity to AC noise, we evaluate both sensitivity measures across the PF and apply the practical filter $\left| \sum_k p_k g_z^{[k]} \right| < 0.1$ as a numerical selection criterion. In fact, most PF points do not satisfy the double-DSS condition, since a point optimized for a single DSS does not necessarily satisfy the stricter double-DSS condition. Accordingly, we adopt different verification thresholds for the single- and double-DSS tests. Under the above filter we obtain approximately 30 double-DSS candidates, three of which achieve $\partial\Omega/\partial\phi_{ac} \sim 10^{-3}$. These candidates lie between DSS-1 and DSS-2 in Fig. 1(a), where both coherence times remain relatively long. Thus, our optimization method not only locates single-DSSs but also reveals regions supporting double-DSSs.

IV. REALIZATION OF QUANTUM GATES

In this section we implement single- and two-qubit gates (e.g., the X and \sqrt{i} SWAP gates) on a fluxonium device operated at a DSS, and evaluate the fidelity improvements under realistic open-system dynamics. In practice, the optimized DSSs appear as isolated points in parameter space rather than continuous manifolds, which complicates gate designs that rely on smoothly traversing operating trajectories. To obtain fast and robust gates we therefore superimpose additional time-dependent control pulses on the periodic-flux background and optimize them using gradient-based optimal-control techniques. This approach mitigates gate infidelity arising from approximations of the Hamiltonian in a rotating frame.

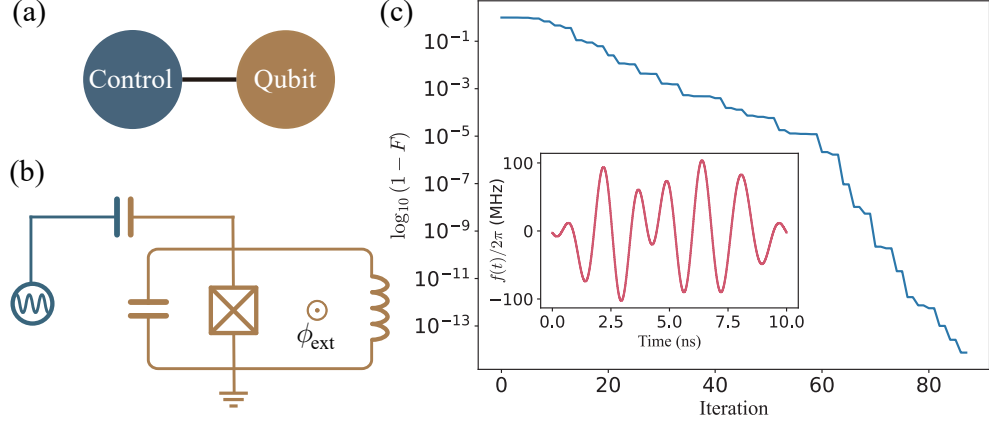


FIG. 2. (a). Control setup for implementing a single-qubit gate in the fluxonium system. (b). The circuit diagram of the device. The system is periodically modulated to stabilize a DSS, while an additional control pulse is applied to steer the system's evolution. (c). Main plot: Closed-system gate fidelity versus GRAPE iteration number for the X gate under periodic flux modulation. Inset: Optimized time-domain control pulse $\Omega_d(t)$ represented using 500 discretized time intervals and constrained to 9 frequency components. The total gate duration is 10 ns, and the pulse amplitude is limited to the range $[-100, 100]$ MHz $\times 2\pi$.

A. Single-Qubit Gate

While the device is held at the DSS, an auxiliary control pulse sequence is applied to implement arbitrary single-qubit rotations. The control schematic is shown in Fig. 2(a) and (b). In the two-level approximation, the total Hamiltonian is

$$H_{\text{total}}(t) = H_q(t) + H_d(t), \quad (21)$$

where the drive term is $H_d(t) = f(t)\sigma_y$ and $f(t)$ denotes the tunable drive amplitude [65]. Moving to the rotating frame defined by the unitary $U_q(t)$ generated by $H_q(t)$, the effective Hamiltonian becomes

$$\begin{aligned} \tilde{H}(t) &= U_q^\dagger(t)H_d(t)U_q(t) \\ &\equiv f(t)\tilde{\sigma}_y(t), \end{aligned} \quad (22)$$

where $\tilde{\sigma}_y(t) = U_q^\dagger(t)\sigma_yU_q(t)$.

For a control duration T , the time-ordered propagator in the rotating frame is $\tilde{U}_T = \mathcal{T} \exp \left(-i \int_0^T \tilde{H}(t) dt \right)$. The control objective is to drive \tilde{U}_T to approximate the target gate U_d . The gate fidelity is

$$F = \left| \frac{1}{d} \langle U_d, \tilde{U}_T \rangle \right|^2, \quad (23)$$

where $d = 2$ is the Hilbert-space dimension and $\langle A, B \rangle = \text{Tr}(A^\dagger B)$. The optimization objective is to minimize the infidelity $L = 1 - F$.

Specifically, the time interval $[0, T]$ is discretized into N uniform steps $t_k = k\Delta t$ ($k = 1, \dots, N$) with $\Delta t = T/N$. Using a first-order Lie-Trotter approximation, the total propagator in the rotating frame is approximated by: $\tilde{U}_T \approx \prod_{k=1}^N \tilde{U}_k = \tilde{U}_N \tilde{U}_{N-1} \dots \tilde{U}_1$, where each step is

$\tilde{U}_k = \exp(-i\tilde{H}(t_k)\Delta t)$ with $\tilde{H}(t_k) = f(t_k)\tilde{\sigma}_y(t_k)$. Here, $f(t_k)$ denotes the discrete drive amplitude, which is optimized by the GRAPE algorithm. To ensure experimental feasibility, we incorporate the following constraints into the optimization: (1) the waveform starts and ends at zero ($f_1 = f_N = 0$), (2) the amplitude is bounded ($|f_k| \leq f_{\text{max}}$), and (3) the control bandwidth is limited. In addition, analytic gradient expressions are used in the optimization, yielding faster convergence than methods based on numerical gradient evaluation.

As an example, we numerically implement the X gate with a total control time of $T = 10$ ns. To impose the bandwidth constraint, the drive is parametrized in the frequency domain by retaining only the first nine terms in its Fourier expansion. The drive amplitude is bounded by $f_{\text{max}} = 100 \times 2\pi$ MHz. Under closed-system dynamics, the optimized waveform achieves fidelity numerically indistinguishable from unity ($F \approx 1$), as shown in main plot in Fig. 2(c). The optimized time-domain pulse is illustrated in subfigure in Fig. 2(c), while the corresponding frequency-domain spectrum is given in FIG. S4(a) in Supplementary Note.

To assess gate robustness of the DSS under decoherence, we evaluate the process fidelity F_χ for the open-system dynamics using the coherence times at the DSS-2. The resulting fidelity is 99.9993%. This process fidelity is defined as

$$F_\chi = \frac{d \text{ Tr}(\chi_T \chi) + \text{Tr}(\chi)}{d+1}, \quad (24)$$

where χ_T is the process matrix of the ideal target gate, χ is the process matrix obtained from the simulated open-system dynamics, and d denotes the Hilbert-space dimension ($d = 2$ for a single qubit). To compute χ , we numerically solve the Lindblad master equation in the

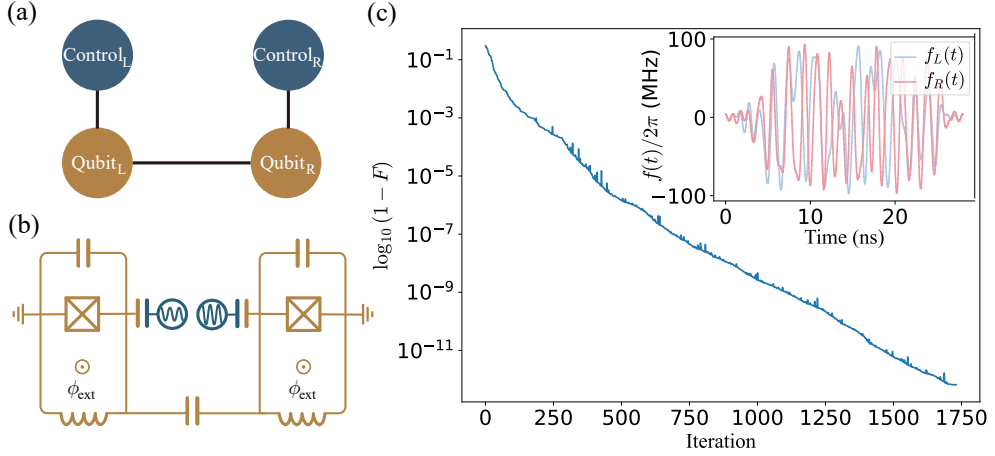


FIG. 3. (a). Schematic of the two-qubit gate implementation between two fluxonium qubits. (b). The circuit diagram of the device. Each qubit is periodically modulated to reach a DSS and is independently driven by an optimized control pulse $f_{L/R}(t)$ acting along the σ_y direction. The interaction between the two qubits is realized through a fixed capacitive coupling term $J\sigma_z\sigma_z$ with $J = 48\text{MHz}$. The form $\sigma_z\sigma_z$ is caused by $R_y(\pi/2)$ between σ_x and σ_z . (c). Main plot: Optimization results for the $\sqrt{i}\text{SWAP}$ gate using the GRAPE algorithm. The main plot shows the gate fidelity versus iteration number during closed-system optimization. Subfigure: The pulse waveforms $f_L(t)$ and $f_R(t)$ in time-domain, each represented using 500 discretized time steps and constrained to a maximum of 31 frequency components. The total evolution time is 28 ns, with pulse amplitudes limited to the range $[-100, 100] \text{ MHz} \times 2\pi$.

rotating frame:

$$\frac{d\tilde{\rho}(t)}{dt} = -i[\tilde{H}(t), \tilde{\rho}(t)] + \sum_{j=1,\phi} \gamma_j \mathcal{D}(L_j) \tilde{\rho}(t), \quad (25)$$

where the dissipator $\mathcal{D}(L)\rho = L\rho L^\dagger - \frac{1}{2}\{L^\dagger L, \rho\}$, and the jump operators are given by $L_1 = \tilde{\sigma}_-$ and $L_\phi = \tilde{\sigma}_z$. The process matrix χ is then reconstructed via quantum process tomography by simulating the channel's action on a complete set of basis operators.

B. Two-Qubit Gate

To implement two-qubit gates, we couple two fluxonium qubits capacitively and apply additional control waveforms to each qubit following the protocol of Ref. [66]. The control configuration is illustrated in Fig. 3(a) and (b). The key distinction of our implementation is that both qubits operate at DSSs. For simplicity, we place both qubits at the same DSS, though the method remains applicable to systems operating at distinct DSSs. In the two-level approximation, the total Hamiltonian is

$$H_{\text{total}}(t) = H_q^L(t) + H_q^R(t) + H_{\text{int}} + H_d^L(t) + H_d^R(t), \quad (26)$$

where $H_q^{L(R)}$ takes the same form as Eq. (3), $H_{\text{int}} = J\sigma_z \otimes \sigma_z$ denotes the capacitive coupling with strength $J = 48 \text{ MHz}$, and the local drives are $H_d^{L(R)}(t) = f_{L(R)}(t)\sigma_y$. The interaction takes the form $\sigma_z \otimes \sigma_z$ due to a $\pi/2$ rotation around the y -axis, under which $\sigma_z \rightarrow \sigma_x$

and $\sigma_x \rightarrow -\sigma_z$. Moving to the rotating frame defined by $U_{rf}(t) = U_q^L(t) \otimes U_q^R(t)$, the effective Hamiltonian becomes

$$\begin{aligned} \tilde{H}(t) &= U_{rf}^\dagger(t) (H_{\text{int}} + H_d^L(t) + H_d^R(t)) U_{rf}(t) \\ &\equiv J\tilde{\sigma}_z^L(t)\tilde{\sigma}_z^R(t) + f_L(t)\tilde{\sigma}_y^L(t) \otimes I + f_R(t)I \otimes \tilde{\sigma}_y^R(t) \end{aligned} \quad (27)$$

where $\tilde{\sigma}_z = U_{rf}^\dagger(t)\sigma_z U_{rf}(t)$. We employ the GRAPE algorithm to optimize the pulse amplitudes $f_L(t_k)$ and $f_R(t_k)$ at each time step in the frequency domain, subject to constraints on both bandwidth and amplitude.

As an example, we numerically implement the $\sqrt{i}\text{SWAP}$ gate with a total control time of $T = 28 \text{ ns}$. Each local control pulse is expanded in the frequency domain using 31 Fourier components to impose the bandwidth limit, and the amplitudes are constrained by $f_{\text{max}} = 100 \times 2\pi \text{ MHz}$. After optimization, the gate achieves a final fidelity numerically indistinguishable from unity under ideal (closed-system) dynamics ($F \approx 1$). Fig. 3(c) illustrates the fidelity convergence across iterations and the corresponding optimized time-domain pulses, and the corresponding frequency spectra are provided in FIG. S4(b) in Supplementary Note. For open-system dynamics, the process fidelity (defined by Eq. (24)) of the optimized gate achieves 99.995%.

V. CONCLUSION

In this work we developed a flux-modulation framework based on general periodic modulation and introduced a Pareto-front (PF) optimization strategy to quan-

tify the trade-off between T_1 and T_ϕ in the presence of low-frequency flux noise and dielectric loss. The resulting PF provides direct access to the maximal values of T_1 and T_ϕ achievable with periodic flux modulation. At the optimal operating points, we design control pulses via external pulse optimization to enable high-fidelity gate operations. In particular, under realistic open-system dynamics and experimental constraints of fluxonium qubits, we demonstrate X and \sqrt{iSWAP} gates with fidelities of 99.9993% and 99.995%, respectively.

These results demonstrate the feasibility of realizing high-coherence quantum control through dynamical modulation. The proposed computational framework is general and extensible, allowing the incorporation of system-specific noise models in future studies. In practice, experimental considerations—such as device anharmonicity—may influence optimal designs. In such cases, preference-based multi-objective optimization can be employed to select PF operating points tailored to specific experimental goals. Moreover, the Pareto-front engineering techniques developed here are broadly applicable and can be extended to other superconducting platforms, including transmon qubits.

ACKNOWLEDGEMENTS

This work was supported by the National Natural Science Foundation of China (Grant No. 92265208,

62173201, U2441217, 92565107), the National Key Research and Development Program of China (Grant No. 2022YFA1405900), and the Innovation Fund of Aerospace Institute 771 (Grant No. 771CX2022003). X.-H. Deng acknowledges support from the Shenzhen Science and Technology Program (KQTD20200820113010023) and the Key-Area Research and Development Program of Guangdong Province (Grant No. 2018B030326001). G. W. Deng acknowledges support from the Sichuan Science and Technology Program (Grant No. 2024YFHZ0372).

AUTHOR CONTRIBUTIONS

Z. Y. performed the main research, derived the proof, wrote the initial draft and prepared all figures. S. J. and Y. H. validated the theory numerically. R.-B. W. proposed the optimization strategy and feasible control designs. Z. Y., X. W., X.-H. D., R.-B. W and G. D. conducted the model analysis. X. W. supervised the project. All authors contributed to manuscript revision and approved the final version.

[1] Y. Nakamura, Y. A. Pashkin, and J. Tsai, *nature* **398**, 786 (1999).

[2] J. E. Mooij, T. P. Orlando, L. Levitov, L. Tian, C. H. van der Wal, and S. Lloyd, *Science* **285**, 1036 (1999).

[3] A. Wallraff, D. I. Schuster, A. Blais, L. Frunzio, R.-S. Huang, J. Majer, S. Kumar, S. M. Girvin, and R. J. Schoelkopf, *Nature* **431**, 162 (2004).

[4] A. Blais, R.-S. Huang, A. Wallraff, S. M. Girvin, and R. J. Schoelkopf, *Phys. Rev. A* **69**, 062320 (2004).

[5] D. Schuster, A. A. Houck, J. Schreier, A. Wallraff, J. Gambetta, A. Blais, L. Frunzio, J. Majer, B. Johnson, M. Devoret, *et al.*, *Nature* **445**, 515 (2007).

[6] J. Koch, T. M. Yu, J. Gambetta, A. A. Houck, D. I. Schuster, J. Majer, A. Blais, M. H. Devoret, S. M. Girvin, and R. J. Schoelkopf, *Phys. Rev. A* **76**, 042319 (2007).

[7] A. A. Houck, H. E. Türeci, and J. Koch, *Nature Physics* **8**, 292 (2012).

[8] D. Riste, M. Dukalski, C. Watson, G. De Lange, M. Tiggelman, Y. M. Blanter, K. W. Lehnert, R. Schouten, and L. DiCarlo, *Nature* **502**, 350 (2013).

[9] M. Gong, M.-C. Chen, Y. Zheng, S. Wang, C. Zha, H. Deng, Z. Yan, H. Rong, Y. Wu, S. Li, F. Chen, Y. Zhao, F. Liang, J. Lin, Y. Xu, C. Guo, L. Sun, J. Clark, H. Wang, C. Peng, C.-Y. Lu, X. Zhu, and J.-W. Pan, *Phys. Rev. Lett.* **122**, 110501 (2019).

[10] F. Arute, K. Arya, R. Babbush, D. Bacon, J. C. Bardin, R. Barends, R. Biswas, S. Boixo, F. G. Brandao, D. A. Buell, *et al.*, *Nature* **574**, 505 (2019).

[11] A. Blais, A. L. Grimsmo, S. M. Girvin, and A. Wallraff, *Rev. Mod. Phys.* **93**, 025005 (2021).

[12] Y. Wu, W.-S. Bao, S. Cao, F. Chen, M.-C. Chen, X. Chen, T.-H. Chung, H. Deng, Y. Du, D. Fan, M. Gong, C. Guo, C. Guo, S. Guo, L. Han, L. Hong, H.-L. Huang, Y.-H. Huo, L. Li, N. Li, S. Li, Y. Li, F. Liang, C. Lin, J. Lin, H. Qian, D. Qiao, H. Rong, H. Su, L. Sun, L. Wang, S. Wang, D. Wu, Y. Xu, K. Yan, W. Yang, Y. Yang, Y. Ye, J. Yin, C. Ying, J. Yu, C. Zha, C. Zhang, H. Zhang, K. Zhang, Y. Zhang, H. Zhao, Y. Zhao, L. Zhou, Q. Zhu, C.-Y. Lu, C.-Z. Peng, X. Zhu, and J.-W. Pan, *Phys. Rev. Lett.* **127**, 180501 (2021).

[13] Z. Ni, S. Li, X. Deng, Y. Cai, L. Zhang, W. Wang, Z.-B. Yang, H. Yu, F. Yan, S. Liu, *et al.*, *Nature* **616**, 56 (2023).

[14] Y. Kim, A. Eddins, S. Anand, K. X. Wei, E. Van Den Berg, S. Rosenblatt, H. Nayfeh, Y. Wu, M. Zaletel, K. Temme, *et al.*, *Nature* **618**, 500 (2023).

[15] S. Bravyi, A. W. Cross, J. M. Gambetta, D. Maslov, P. Rall, and T. J. Yoder, *Nature* **627**, 778 (2024).

[16] *Nature* **638**, 920 (2025).

[17] H. Puterman, K. Noh, C. T. Hann, G. S. MacCabe, S. Aghaeimeibodi, R. N. Patel, M. Lee, W. M. Jones, H. Moradinejad, R. Rodriguez, *et al.*, *Nature* **638**, 927 (2025).

[18] V. E. Manucharyan, J. Koch, L. I. Glazman, and M. H. Devoret, *Science* **326**, 113 (2009).

[19] L. B. Nguyen, Y.-H. Lin, A. Somoroff, R. Mencia, N. Grabon, and V. E. Manucharyan, *Phys. Rev. X* **9**, 041041 (2019).

[20] L. B. Nguyen, G. Koolstra, Y. Kim, A. Morvan, T. Chistolini, S. Singh, K. N. Nesterov, C. Jünger, L. Chen, Z. Pedramrazi, B. K. Mitchell, J. M. Kreikebaum, S. Puri, D. I. Santiago, and I. Siddiqi, *PRX Quantum* **3**, 037001 (2022).

[21] B. M. Terhal, *Rev. Mod. Phys.* **87**, 307 (2015).

[22] A. G. Fowler, M. Mariantoni, J. M. Martinis, and A. N. Cleland, *Phys. Rev. A* **86**, 032324 (2012).

[23] J. Preskill, *Quantum* **2**, 79 (2018).

[24] K. Temme, S. Bravyi, and J. M. Gambetta, *Phys. Rev. Lett.* **119**, 180509 (2017).

[25] F. Yoshihara, K. Harrabi, A. O. Niskanen, Y. Nakamura, and J. S. Tsai, *Phys. Rev. Lett.* **97**, 167001 (2006).

[26] J. M. Martinis, K. B. Cooper, R. McDermott, M. Steffen, M. Ansmann, K. D. Osborn, K. Cicak, S. Oh, D. P. Papas, R. W. Simmonds, and C. C. Yu, *Phys. Rev. Lett.* **95**, 210503 (2005).

[27] G. Ithier, E. Collin, P. Joyez, P. J. Meeson, D. Vion, D. Esteve, F. Chiarello, A. Shnirman, Y. Makhlin, J. Schriefl, and G. Schön, *Phys. Rev. B* **72**, 134519 (2005).

[28] J. Koch, T. M. Yu, J. Gambetta, A. A. Houck, D. I. Schuster, J. Majer, A. Blais, M. H. Devoret, S. M. Girvin, and R. J. Schoelkopf, *Phys. Rev. A* **76**, 042319 (2007).

[29] L. B. Nguyen, Y.-H. Lin, A. Somoroff, R. Mencia, N. Grabon, and V. E. Manucharyan, *Phys. Rev. X* **9**, 041041 (2019).

[30] H. Zhang, S. Chakram, T. Roy, N. Earnest, Y. Lu, Z. Huang, D. K. Weiss, J. Koch, and D. I. Schuster, *Phys. Rev. X* **11**, 011010 (2021).

[31] E. A. Sete, M. J. Reagor, N. Didier, and C. T. Rigetti, *Phys. Rev. Appl.* **8**, 024004 (2017).

[32] L. Viola, E. Knill, and S. Lloyd, *Phys. Rev. Lett.* **82**, 2417 (1999).

[33] K. Khodjasteh and D. A. Lidar, *Phys. Rev. Lett.* **95**, 180501 (2005).

[34] L. Cywiński, R. M. Lutchyn, C. P. Nave, and S. Das Sarma, *Phys. Rev. B* **77**, 174509 (2008).

[35] G. S. Uhrig, *Phys. Rev. Lett.* **98**, 100504 (2007).

[36] B. Pokharel, N. Anand, B. Fortman, and D. A. Lidar, *Phys. Rev. Lett.* **121**, 220502 (2018).

[37] C. Wang, C. Axline, Y. Y. Gao, T. Brecht, Y. Chu, L. Frunzio, M. H. Devoret, and R. J. Schoelkopf, *Applied Physics Letters* **107**, 162601 (2015).

[38] N. Didier, E. A. Sete, J. Combes, and M. P. da Silva, *Phys. Rev. Appl.* **12**, 054015 (2019).

[39] J. A. Valery, S. Chowdhury, G. Jones, and N. Didier, *PRX Quantum* **3**, 020337 (2022).

[40] Z. Huang, P. S. Mundada, A. Gyenis, D. I. Schuster, A. A. Houck, and J. Koch, *Phys. Rev. Appl.* **15**, 034065 (2021).

[41] P. S. Mundada, A. Gyenis, Z. Huang, J. Koch, and A. A. Houck, *Phys. Rev. Appl.* **14**, 054033 (2020).

[42] A. Gandon, C. Le Calonnec, R. Shillito, A. Petrescu, and A. Blais, *Phys. Rev. Appl.* **17**, 064006 (2022).

[43] J.-M. Cheng, Y.-C. Zhang, X.-F. Zhou, and Z.-W. Zhou, *New Journal of Physics* **24**, 123034 (2022).

[44] J. Lauwens, K. Moors, and B. Sorée, Optimization of floquet fluxonium qubits with commensurable two-tone drives (2025), arXiv:2506.06002 [cond-mat.mes-hall].

[45] A. Frees, S. Mehl, J. K. Gamble, M. Friesen, and S. Coppersmith, *npj Quantum Information* **5**, 73 (2019).

[46] Q. Guo, S.-B. Zheng, J. Wang, C. Song, P. Zhang, K. Li, W. Liu, H. Deng, K. Huang, D. Zheng, *et al.*, *Physical review letters* **121**, 130501 (2018).

[47] J.-M. Pirkkalainen, S. Cho, J. Li, G. Paraoanu, P. Hakonen, and M. Sillanpää, *Nature* **494**, 211 (2013).

[48] D. D. Briseño-Colunga, B. Bhandari, D. Das, L. B. Nguyen, Y. Kim, D. I. Santiago, I. Siddiqi, A. N. Jordan, and J. Dressel, *Dynamical sweet and sour regions in bichromatically driven floquet qubits* (2025), arXiv:2505.22606 [quant-ph].

[49] V. E. Manucharyan, J. Koch, L. I. Glazman, and M. H. Devoret, *Science* **326**, 113 (2009).

[50] S. Kohler, T. Dittrich, and P. Hänggi, *Phys. Rev. E* **55**, 300 (1997).

[51] C. Creffield, *Phys. Rev. B* **67**, 165301 (2003).

[52] G. Suárez and M. Horodecki, *Making non-markovian master equations accessible with approximate environments* (2025), arXiv:2506.22346 [quant-ph].

[53] V. E. Manucharyan, N. A. Masluk, A. Kamal, J. Koch, L. I. Glazman, and M. H. Devoret, *Phys. Rev. B* **85**, 024521 (2012).

[54] P. V. Klimov, J. Kelly, Z. Chen, M. Neeley, A. Megrant, B. Burkett, R. Barends, K. Arya, B. Chiaro, Y. Chen, A. Dunsworth, A. Fowler, B. Foxen, C. Gidney, M. Giustina, R. Graff, T. Huang, E. Jeffrey, E. Lucero, J. Y. Mutus, O. Naaman, C. Neill, C. Quintana, P. Roushan, D. Sank, A. Vainsencher, J. Wenner, T. C. White, S. Boixo, R. Babbush, V. N. Smelyanskiy, H. Neven, and J. M. Martinis, *Phys. Rev. Lett.* **121**, 090502 (2018).

[55] P. Groszkowski, A. Di Paolo, A. L. Grimsmo, A. Blais, D. I. Schuster, A. A. Houck, and J. Koch, *New Journal of Physics* **20**, 043053 (2018).

[56] A. Kou, W. C. Smith, U. Vool, R. T. Brierley, H. Meier, L. Frunzio, S. M. Girvin, L. I. Glazman, and M. H. Devoret, *Phys. Rev. X* **7**, 031037 (2017).

[57] K. Deb, A. Pratap, S. Agarwal, and T. Meyarivan, *IEEE Transactions on Evolutionary Computation* **6**, 182 (2002).

[58] E. Zitzler, M. Laumanns, and L. Thiele, *TIK report* **103** (2001).

[59] K. Li, R. Chen, G. Fu, and X. Yao, *IEEE Transactions on Evolutionary Computation* **23**, 303 (2018).

[60] E. Zitzler and S. Künzli, in *Parallel Problem Solving from Nature - PPSN VIII* (Springer Berlin Heidelberg, Berlin, Heidelberg, 2004) pp. 832–842.

[61] J. Bader and E. Zitzler, *Evolutionary computation* **19**, 45 (2011).

[62] Q. Zhang and H. Li, *Trans. Evol. Comp* **11**, 712–731 (2007).

[63] S.-Z. Zhao, P. N. Suganthan, and Q. Zhang, *IEEE Transactions on Evolutionary Computation* **16**, 442 (2012).

[64] ColaLab, *Emoc: Evolutionary multi-objective optimization in c++*.

[65] P. Krantz, M. Kjaergaard, F. Yan, T. P. Orlando, S. Gustavsson, and W. D. Oliver, *Applied Physics Reviews* **6**, 021318 (2019).

[66] K. N. Nesterov, C. Wang, V. E. Manucharyan, and M. G. Vavilov, *Phys. Rev. Appl.* **18**, 034063 (2022).

[67] E. Zitzler and S. Künzli, in *Proc. of the 8th International Conference on Parallel Problem Solving from Nature (PPSN VIII)* (2004) pp. 832–842.

[68] Q. Zhang and H. Li, *IEEE Transactions on Evolutionary Computation* **11**, 712 (2007).

[69] Y. Song, J. Li, Y.-J. Hai, Q. Guo, and X.-H. Deng, *Phys. Rev. A* **105**, 012616 (2022).

[70] N. Didier, *Flux control of superconducting qubits at dynamical sweet spots* (2019), arXiv:1912.09416 [quant-ph].

[71] M. Thibodeau, A. Kou, and B. K. Clark, *PRX Quantum* **5**, 040314 (2024).

Supplemental Material for Pareto-Front Engineering of Dynamical Sweet Spots in Superconducting Qubits

VI. PARETO FRONTS

The PFs obtained with four different selection strategies are shown in Fig. S1; these correspond to Fig. 1(a) in the main text. In region C_1 , SPEA2 and tDEA achieve the most comprehensive coverage. In region C_2 , all four algorithms perform well and yield broadly similar results. Region C_3 is sampled predominantly by ENS-MOEA/D, while the other methods contribute little coverage there. The locations of the three DSSs listed in Table I are marked in each subfigure, and their corresponding periodic flux-modulation parameters are given in Table I.

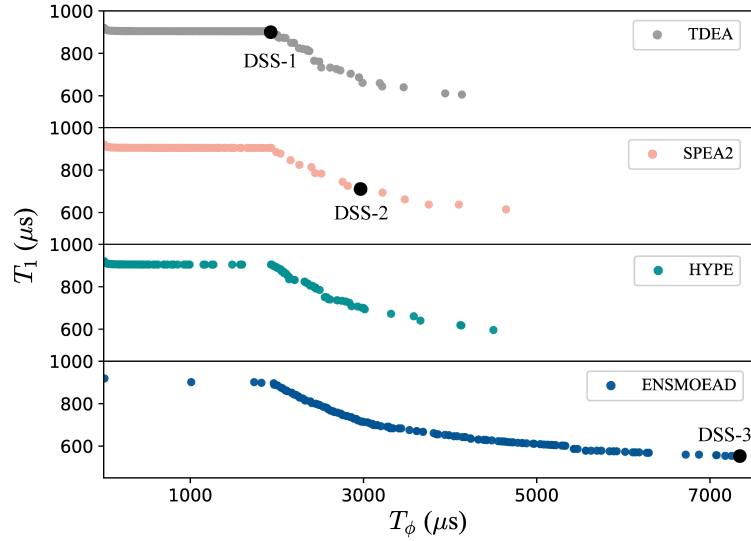


FIG. S1. Pareto fronts obtained using four different multi-objective selection strategies (tDEA, SPEA2, ENS-MOEA/D, and HypE) under Fourier truncation length $n = 4$. Each PF represents the trade-off between T_1 and T_ϕ optimized via the periodic function $P(t)$. The positions of three representative dynamical sweet spots (DSS 1–3), also listed in Table I, are marked in each subfigure. All optimization runs were performed for 2000 iterations.

Parameter	DSS-1	DSS-2	DSS-3
p_0	0.23	0.69	0.37
p_1	$-0.55 + 0.21i$	$0.73 - 0.99i$	$-0.99 - i$
p_2	$0.96 - 0.95i$	$0.97 - 0.88i$	$0.01 - 0.87i$
p_3	$-0.58 + 0.31i$	$0.28 + 0.84i$	$-0.99 + 0.99i$
p_4	$0.14 - 0.85i$	$-0.16 + 0.58i$	$0.99 + i$
ω_d	$1.01\Omega_{ge}$	$1.13\Omega_{ge}$	$0.99\Omega_{ge}$
Method	tDEA	SPEA2	ENSMOEA/D

TABLE I. Modulation parameters corresponding to three representative dynamical working points identified by different optimization strategies. These parameters determine the time-dependent flux modulation function $P(t)$ that identifies a DSS.

We employed the same four selection strategies to optimize T_1 and T_ϕ while varying the parameter length n of the periodic function $P(t)$. Each strategy was run for up to 2000 iterations; the resulting PFs are shown in Fig. S2. For all tested values of n , the PFs lie in the ranges $T_\phi \in [2000, 4000]$ and $T_1 \in [600, 800]$. The attainable maximum T_1 generally increases with n . Notably, the maximal T_ϕ observed at $n = 5$ is lower than that reported for $n = 4$ in

Fig. 1 of the main text. We attribute this discrepancy to incomplete convergence at $n = 5$: enlarging n increases the dimensionality and complexity of the parameter space, which typically requires more iterations to reach comparable convergence. Due to computational-resource limits we did not extend the optimizations for larger n . It is expected that further improvements in the maximum achievable T_ϕ may be obtained with larger n .

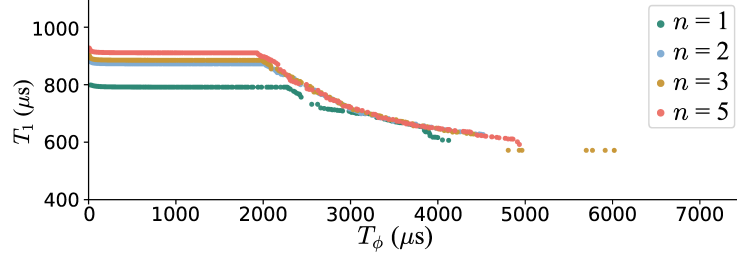


FIG. S2. Comparison of Pareto fronts obtained under different Fourier truncation lengths $n = 1$ to 5 for the periodic modulation function $P(t)$. All four selection strategies were applied for each n , with a maximum of 2000 optimization iterations. As n increases, the PFs become broader and more expressive, and higher values of T_1 are observed. However, the case $n = 5$ exhibits lower maximum T_ϕ than the $n = 4$ case (main text Fig. 1).

VII. NUMERICAL ERRORS INDUCED BY FLOQUET MATRIX TRUNCATION

In this section we quantify the numerical errors introduced by truncating the Floquet matrix \mathcal{H}_F . As shown in section II.B in main text, the decoherence rates $\gamma_{\pm,z}$ depend on the Floquet states $|\omega_{\pm}(t)\rangle$ and their quasienergies ϵ_{\pm} ; consequently, the accuracy of the computed decoherence rates is governed by the numerical precision of these Floquet quantities. We adopt a truncation-free reference Floquet basis $|\omega_{\pm}^U(t)\rangle$, obtained by diagonalizing the propagator $U_q(t)$ (i.e. the time-ordered evolution operator over one drive period) [51]. This avoids constructing or truncating \mathcal{H}_F and is limited only by the numerical accuracy of the differential-equation solver, so we use it to quantify truncation-induced errors.

We quantify truncation error using the fidelity $F = |\langle \omega_{\pm}^U(0) | \omega_{\pm}^H(0) \rangle|$, where $|\omega_{\pm}^H(0)\rangle$ is obtained by diagonalizing the truncated Floquet matrix \mathcal{H}_F with truncation dimension K_{\max} , and $|\omega_{\pm}^U(0)\rangle$ is the truncation-free reference state. When the parameter length n of the periodic function $P(t)$ increases, the Floquet matrix acquires more nonzero blocks, which can lead to larger truncation-induced errors. We therefore compute the fidelity under different truncation settings to characterize this effect. The numerical results are plotted in Fig. S3. The infidelity $1 - F$ drops below 10^{-10} once the truncation dimension satisfies $K_{\max} = 3n$.

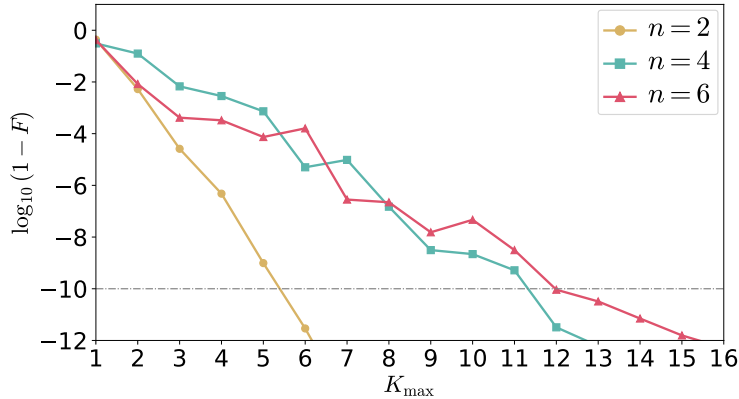


FIG. S3. Numerical fidelity between the Floquet state $|\omega_{\pm}^H(0)\rangle$ and the reference Floquet state $|\omega_{\pm}^U(0)\rangle$. The infidelity quantifies the truncation-induced error for different truncation dimensions K_{\max} . The numerical error decreases exponentially with increasing K_{\max} , and falls below 10^{-10} when $K_{\max} \geq 3n$, justifying the truncation setting used in the main text.

VIII. THE FREQUENCY SPECTRA OF THE OPTIMIZED PULSES

To enhance the experimental feasibility of the optimized pulses used for gate realization, we impose three constraints in sequence. First, to ensure the waveform vanishes smoothly at the boundaries, we multiply the waveform by a smooth window function $W(t) = \sin^2(\pi t/T)$ (for $t \in [0, T]$). Second, to bound the instantaneous amplitude we apply a scaled sigmoid $\sigma_s(x) = A(2\sigma(Bx) - 1)$ (with chosen scale parameters A, B) pointwise to the waveform to enforce amplitude limits. The scaling parameters A, B are chosen so that $|\sigma_s(x)| \leq f_{\max}$. Third, to limit the bandwidth the waveform is transformed to the frequency domain and all spectral components with indices $|n| > N_c$ are set to zero. The frequency spectra of the control pulses used to realize the X and $\sqrt{i\text{SWAP}}$ gates are shown in Fig. S4 (a) and (b), respectively.

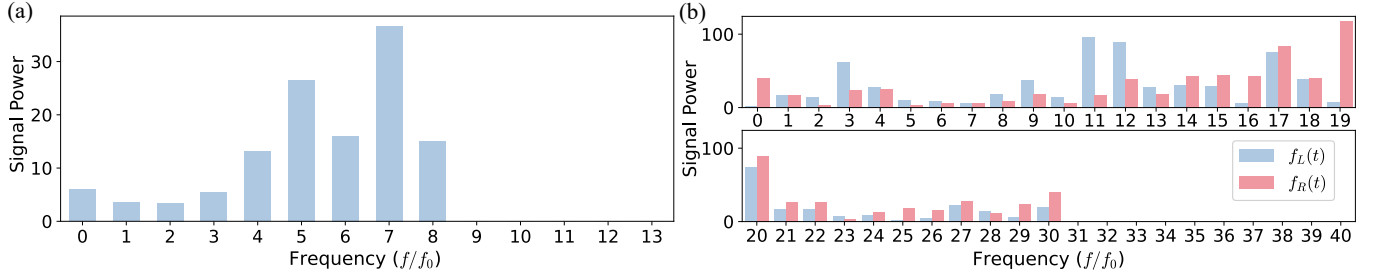


FIG. S4. (a). Normalized frequency spectrum of the optimized control pulse used to implement the X gate. The frequency f is normalized by the base frequency $f_0 = 1/T$, where $T = 10$ ns is the total pulse duration. (b). Normalized frequency spectra of the optimized control pulses used for the $\sqrt{i\text{SWAP}}$ gate.

IX. PROOF OF THEOREM 1

In this appendix we prove a lower bound on γ_1 , which yields an upper bound on T_1 . Substituting the expression of γ_{\pm} in Eq.(13) in main text, the γ_1 takes the form,

$$\begin{aligned} \gamma_1 &= \sum_{k \in \mathbb{Z}} |g_+^{[k]}|^2 S(k\omega_d - \Omega) + \sum_{k \in \mathbb{Z}} |g_-^{[k]}|^2 S(k\omega_d + \Omega) \\ &= \sum_{k \in \mathbb{Z}} |g_+^{[k]}|^2 (S(k\omega_d - \Omega) + S(-k\omega_d + \Omega)) \\ &\equiv \sum_{k \in \mathbb{Z}} |g_+^{[k]}|^2 \tilde{S}(k\omega_d - \Omega). \end{aligned} \quad (\text{S1})$$

In the second equation we use $|g_+^{[k]}| = |g_-^{[-k]}|$. The function $\tilde{S}(\omega)$ is defined as $\tilde{S}(\omega) = S(\omega) + S(-\omega)$. Based on Eq.(12) in main text and inequality $A + B \geq 2\sqrt{AB}$, $\tilde{S}(\omega)$ can be scaled as

$$\tilde{S}(\omega) = \frac{4\pi A_f^2}{|\omega|} + \frac{A_d \omega^2}{4\pi^2} \geq \frac{2}{\sqrt{\pi}} A_f (A_d |\omega|)^{\frac{1}{2}}. \quad (\text{S2})$$

The inequality (S1) becomes

$$\gamma_1 \geq \frac{2}{\sqrt{\pi}} A_f \sqrt{A_d} \cdot \sum_{k \in \mathbb{Z}} |g_+^{[k]}|^2 |k\omega_d - \Omega|^{\frac{1}{2}}. \quad (\text{S3})$$

The minimal value of set $\{|k\omega_d - \Omega|^{\frac{1}{2}} \mid k \in \mathbb{Z}\}$ represents

$$\sqrt{\omega_d} \cdot \min_{k \in \mathbb{Z}} \sqrt{\left|k - \frac{\Omega}{\omega_d}\right|} \equiv \sqrt{\omega_d} \left\| \frac{\Omega}{\omega_d} \right\|_{\mathbb{R}/\mathbb{Z}}^{\frac{1}{2}} \quad (\text{S4})$$

where $\|x\|_{\mathbb{R}/\mathbb{Z}}$ refers to the distance between x and the nearest integer, i.e., $\|x\|_{\mathbb{R}/\mathbb{Z}} = \min_{k \in \mathbb{Z}} |x - k|$. Therefore, the inequality (S3) can be scaled as

$$\gamma_1 \geq \frac{2}{\sqrt{\pi}} A_f \sqrt{A_d \omega_d} \left\| \frac{\Omega}{\omega_d} \right\|_{\mathbb{R}/\mathbb{Z}}^{\frac{1}{2}} \sum_{k \in \mathbb{Z}} \left| g_+^{[k]} \right|^2 \quad (\text{S5})$$

with result that

$$T_1 \leq \frac{\sqrt{\pi}}{2A_f \sqrt{A_d \omega_d} \left\| \frac{\Omega}{\omega_d} \right\|_{\mathbb{R}/\mathbb{Z}}^{\frac{1}{2}} \sum_{k \in \mathbb{Z}} \left| g_+^{[k]} \right|^2}. \quad (\text{S6})$$

This upper bound of T_1 holds for any periodic flux drive system.

If the system is operated in a DSS, the upper bound can be further simplified into a form independent of the filter weights. Since $\sum_{k \in \mathbb{Z}} \left| g_+^{[k]} \right|^2 = 1 - \sum_{k \in \mathbb{Z}} \left| g_z^{[k]} \right|^2$, the inequality (S6) becomes

$$T_1 \leq \frac{\sqrt{\pi}}{2A_f \sqrt{A_d \omega_d} \left\| \frac{\Omega}{\omega_d} \right\|_{\mathbb{R}/\mathbb{Z}}^{\frac{1}{2}} \left| 1 - \sum_{k \in \mathbb{Z}} \left| g_z^{[k]} \right|^2 \right|}. \quad (\text{S7})$$

where condition $\sum_{k \in \mathbb{Z}} \left| g_+^{[k]} \right|^2 > 0$ is used. Next, we estimate the upper bound of $\sum_k \left| g_z^{[k]} \right|^2$. Let $f(t) = \text{Tr}[\sigma_z \tau_z(t)]$. Using integration by parts for $g_z^{[k]}$ in Eq.(10) in main text, it takes the form

$$\begin{aligned} g_z^{[k]} &= \frac{1}{2T} \int_0^T f(t) e^{ik\omega_d t} dt \\ &= \frac{1}{2ik\omega_d} \frac{1}{T} \left(f(t) e^{ik\omega_d t} \Big|_0^T - \int_0^T f'(t) e^{ik\omega_d t} dt \right) \\ &= \frac{i}{2k\omega_d} \frac{1}{T} \int_0^T f'(t) e^{ik\omega_d t} dt, \end{aligned} \quad (\text{S8})$$

where we used the periodicity $f(t+T) = f(t)$ in the last step. According to the Cauchy-Schwarz inequality in L^2 , we obtain the following bound on $\left| g_z^{[k]} \right|$:

$$\begin{aligned} \left| g_z^{[k]} \right| &\leq \frac{1}{2|k|\omega_d} \left(\frac{1}{T} \int_0^T |f'(t)|^2 dt \right)^{1/2} \left(\frac{1}{T} \int_0^T |e^{2ik\omega_d t}| dt \right)^{1/2} \\ &= \frac{1}{2|k|\omega_d} \left(\frac{1}{T} \int_0^T |f'(t)|^2 dt \right)^{1/2} \\ &\leq \frac{1}{2|k|\omega_d} |f'_{\max}|. \end{aligned} \quad (\text{S9})$$

Therefore, the total weights $\sum_k \left| g_z^{[k]} \right|^2$ satisfies

$$\sum_k \left| g_z^{[k]} \right|^2 \leq \sum_k \frac{1}{4k^2\omega_d^2} |f'_{\max}|^2 = \frac{\pi^2}{3} \cdot \frac{1}{4\omega_d^2} |f'_{\max}|^2, \quad (\text{S10})$$

where we use condition that $\left| g_z^{[0]} \right| \approx 0$ in DSS. We next compute $|f'_{\max}|$. The Floquet states can be expressed as

$$|w_{\pm}(t)\rangle = e^{i\epsilon_{\pm}t} U(t) |w_{\pm}(0)\rangle \quad (\text{S11})$$

where $U(t)$ is generated by the Hamiltonian given in Eq. (3) in main text, expressed as [40],

$$\begin{aligned} U(t) &= \mathcal{T} \exp \left[-i \int_0^t H_q(t') dt' \right] \\ &= \sum_{j=\pm} |w_j(t)\rangle \langle w_j(0)| \exp(-i\epsilon_j t) \end{aligned} \quad (\text{S12})$$

Substituting this expression into $f(t)$, we obtain

$$\begin{aligned} f(t) &= \text{Tr} [\sigma_z (|w_+(t)\rangle \langle w_+(t)| - |w_-(t)\rangle \langle w_-(t)|)] \\ &= \text{Tr} [\sigma_z U(t) (|w_+(0)\rangle \langle w_+(0)| \\ &\quad - |w_-(0)\rangle \langle w_-(0)|) U^\dagger(t)] \\ &= \text{Tr} [U^\dagger(t) \sigma_z U(t) \cdot \tau_z(0)]. \end{aligned} \quad (\text{S13})$$

Its derivative is

$$\begin{aligned} \frac{d}{dt} f(t) &= \text{Tr} \left[\left(\frac{d}{dt} U^\dagger(t) \sigma_z U(t) + U^\dagger(t) \sigma_z \frac{d}{dt} U(t) \right) \tau_z(0) \right] \\ &= \text{Tr} \left[(iU^\dagger(t) H(t) \sigma_z U(t) - iU^\dagger(t) \sigma_z H(t) U(t)) \tau_z(0) \right] \\ &= \text{Tr} \left[(iU^\dagger(t) [H(t), \sigma_z] U(t)) \tau_z(0) \right] \\ &= \text{Tr} \left[(\Delta U^\dagger(t) \sigma_y U(t)) \tau_z(0) \right]. \end{aligned} \quad (\text{S14})$$

where we used $[H(t), \sigma_z] = i\Delta\sigma_y$ and $H(t) = \frac{\Delta}{2}\sigma_x + \left(\frac{B}{2} + AP(t)\right)\sigma_z$. Using the Cauchy-Schwarz inequality for the trace, we find

$$\begin{aligned} \frac{d}{dt} f(t) &\leq \sqrt{\text{Tr} [(-\Delta U^\dagger(t) \sigma_y U(t))^\dagger (-\Delta U^\dagger(t) \sigma_y U(t))]} \\ &\quad \times \sqrt{\text{Tr} [\tau_z(0)^\dagger \tau_z(0)]} \\ &= \sqrt{\text{Tr} [\Delta^2 \sigma_y^\dagger \sigma_y]} \sqrt{2} \\ &= 2\Delta. \end{aligned} \quad (\text{S15})$$

Substituting this into Eq. (S10), we obtain

$$\sum_k |g_z^{[k]}|^2 \leq \frac{\pi^2}{3} \cdot \frac{\Delta^2}{\omega_d^2}. \quad (\text{S16})$$

Based on this result, inequality (S7) can be scaled as

$$T_1 \leq \frac{3\sqrt{\pi}\omega_d^2}{2A_f (A_d\omega_d)^{\frac{1}{2}} \left\| \frac{\Omega}{\omega_d} \right\|_{\mathbb{R}/\mathbb{Z}}^{\frac{1}{2}} |3\omega_d^2 - \pi^2\Delta^2|}. \quad (\text{S17})$$

X. EQUIVALENT CONDITIONS FOR DOUBLE DYNAMICAL SWEET SPOT

In this section we derive an equivalent condition for identifying a double DSS. Condition $\partial\Omega/\partial\phi_{\text{dc}} \approx 0$ was shown in Ref. [40] to be equivalent to $|g_z^{[0]}| \approx 0$. Here we focus on the analogous formulation of the condition $\partial\Omega/\partial\phi_{\text{ac}} \approx 0$. Noting that $A \propto \phi_{\text{ac}}$, it suffices to examine the sensitivity of the quasienergy gap with respect to A , i.e. $\partial\Omega/\partial A$.

Since the quasienergies ϵ_j satisfy the Floquet eigenvalue equation, they can be expressed as

$$\begin{aligned}\epsilon_j &= \langle \omega_j(t) | H_{\mathcal{F}} | \omega_j(t) \rangle \\ &= \frac{\omega_d}{2\pi} \int_0^{2\pi/\omega_d} dt \langle \omega_j(t) | H_{\mathcal{F}} | \omega_j(t) \rangle,\end{aligned}\tag{S18}$$

where $H_{\mathcal{F}} = H_q(t) - i \frac{\partial}{\partial t}$ is the Floquet matrix. Consider a perturbation term $\delta AP(t)\sigma_z$, which modifies the Floquet matrix to $H'_{\mathcal{F}} = H_{\mathcal{F}} + \delta AP(t)\sigma_z$. According to first-order perturbation theory,

$$\begin{aligned}\delta\epsilon_j &= \frac{\omega_d}{2\pi} \int_0^{2\pi/\omega_d} dt \langle \omega_j(t) | \delta AP(t)\sigma_z | \omega_j(t) \rangle \\ &= \delta A \cdot \frac{\omega_d}{2\pi} \int_0^{2\pi/\omega_d} dt P(t) \langle \omega_j(t) | \sigma_z | \omega_j(t) \rangle.\end{aligned}\tag{S19}$$

The resulting variation in the quasienergy difference is

$$\begin{aligned}\delta\Omega &= \delta A \cdot \frac{\omega_d}{2\pi} \int_0^{2\pi/\omega_d} dt P(t) (\langle \omega_1(t) | \sigma_z | \omega_1(t) \rangle \\ &\quad - \langle \omega_0(t) | \sigma_z | \omega_0(t) \rangle) \\ &= \delta A \cdot \sum_{k=-\infty}^{\infty} p_k \cdot \frac{\omega_d}{2\pi} \int_0^{2\pi/\omega_d} dt \text{Tr}[\sigma_z \tau_z(t)] e^{ik\omega_d t} \\ &= \delta A \cdot \sum_{k=-\infty}^{\infty} p_k \cdot g_z^{[k]},\end{aligned}\tag{S20}$$

which gives $\frac{\partial\Omega}{\partial A} = \sum_{k=-\infty}^{\infty} p_k g_z^{[k]}$. The equivalent condition for a double DSS can be expressed as

$$\left| g_z^{[0]} \right| \approx 0, \quad \sum_k p_k g_z^{[k]} \approx 0.\tag{S21}$$